nature photonics

ARTICLES

PUBLISHED ONLINE: 29 JUNE 2014 | DOI: 10.1038/NPHOTON.2014.138

Integrated flexible chalcogenide glass photonic devices

Lan Li[1†], Hongtao Lin[1†], Shutao Qiao[2†], Yi Zou[1], Sylvain Danto[3], Kathleen Richardson[3,4], J. David Musgraves[4], Nanshu Lu[2] and Juejun Hu[1*]

Photonic integration on thin flexible plastic substrates is important for emerging applications ranging from the realization of flexible interconnects to conformal sensors applied to the skin. Such devices are traditionally fabricated using pattern transfer, which is complicated and has limited integration capacity. Here, we report a convenient monolithic approach to realize flexible, integrated high-index-contrast chalcogenide glass photonic devices. By developing local neutral axis designs and suitable fabrication techniques, we realize a suite of photonic devices including waveguides, microdisk resonators, add–drop filters and photonic crystals that have excellent optical performance and mechanical flexibility, enabling repeated bending down to sub-millimetre radii without measurable performance degradation. The approach offers a facile fabrication route for three-dimensional high-index-contrast photonics that are difficult to create using traditional methods.

Conventional on-chip photonic devices are fabricated almost exclusively on rigid substrates with little mechanical flexibility, but integration on deformable polymer substrates has given birth to flexible photonics, a field that has emerged rapidly in recent years to become the forefront of photonics research. By imparting mechanical flexibility to planar photonic structures, the technology has enormous application potential for aberration-free optical imaging[1], epidermal sensing[2], chip-to-chip interconnects[3] and broadband photonic tuning[4]. Free-space-coupled optical components including photodetectors[5], light-emitting diodes[6] and Fano reflectors[7] are among the first flexible semiconductor photonic devices to have been demonstrated. Planar integrated photonic structures such as microresonators and other waveguide-integrated devices potentially offer significantly improved performance characteristics compared to their free-space counterparts, because of their tight optical confinement and the facilitation of essential components for integrated photonic circuits. To date, flexible planar photonic devices have been fabricated almost exclusively using polymeric materials, which do not have the high refractive indices necessary for strong optical confinement. Silicon-based, high-index-contrast flexible waveguide devices were first demonstrated using a transfer printing approach[8]. However, this hybrid approach involves multiple pattern transfer steps between different substrates and has limited throughput, yield and integration capacity[9,10]. More recently, amorphous silicon devices have been fabricated via direct deposition and patterning[11]. However, the optical quality of the silicon material was severely compromised by the low deposition temperature dictated by the polymer substrate's thermal budget. Silicon nitride is another material candidate that does not require epitaxial growth on single-crystal substrates. However, polymer substrates cannot withstand the high deposition temperature of low-loss nitride in the low-pressure chemical vapour deposition process (>500 °C)[12], and silicon nitride deposited by sputtering or plasma-enhanced chemical vapour deposition (PECVD) generally exhibits high optical losses[13,14]. Oxynitride deposited via PECVD or sputtering may offer a viable route for flexible photonic device fabrication, although oxygen plasma damage to polymer substrates presents a challenge yet to be mitigated.

As well as these multimaterial integration challenges, planar integrated photonics stipulate a distinctively different set of requirements in their configurational design to achieve structural flexibility. For example, the neutral plane design widely adopted for flexible electronics[15,16] dictates that the device layer should be embedded inside the flexible substrate near the neutral plane to minimize strain exerted on the devices when the structure is deformed. However, encapsulation of the various photonic components deep within a thick top cladding layer prohibits effective heat dissipation as well as evanescent wave interactions with the external environment, an essential condition for biochemical sensing and evanescent optical coupling. To achieve efficient optical coupling, current flexible photonic devices are placed on the surface of polymer substrates. As a consequence, the devices are subjected to large strains upon bending and exhibit only moderate flexibility with a bending radius typically no less than 5 mm (refs 3,5,11). This mechanical performance severely limits the range of degrees of freedom available for deployment.

In this Article, we demonstrate monolithic photonic integration on plastic substrates using high-refractive-index chalcogenide glass (ChG) materials. This process yields high-index-contrast photonic devices with record optical performance and benefits significantly from improved processing protocols based on simple, low-cost contact lithography. We show that this versatile process can be readily adapted to different glass compositions with tailored optical properties to meet different candidate applications. A novel local-neutral-axis design is implemented to render the structure highly mechanically flexible, enabling repeated bending of the devices down to sub-millimetre bending radii without a measurable degradation in optical performance. We note that classical multilayer beam bending theory fails in our design due to the large modulus contrast among the different layers. For this reason, a new analytical model was developed to take into account the multiple neutral axes in a multilayer stack so as to successfully

[1]Department of Materials Science and Engineering, University of Delaware, Newark, Delaware 19716, USA, [2]Centre for Mechanics of Solids, Structures and Materials, Department of Aerospace Engineering and Engineering Mechanics, University of Texas at Austin, Austin, Texas 78712, USA, [3]College of Optics and Photonics, CREOL, Department of Materials Science and Engineering, University of Central Florida, Orlando, Florida 32816, USA, [4]IRradiance Glass Inc., Orlando, Florida 32828, USA; †These authors contributed equally to this work. *e-mail: hujuejun@udel.edu

© 2014 Macmillan Publishers Limited. All rights reserved.

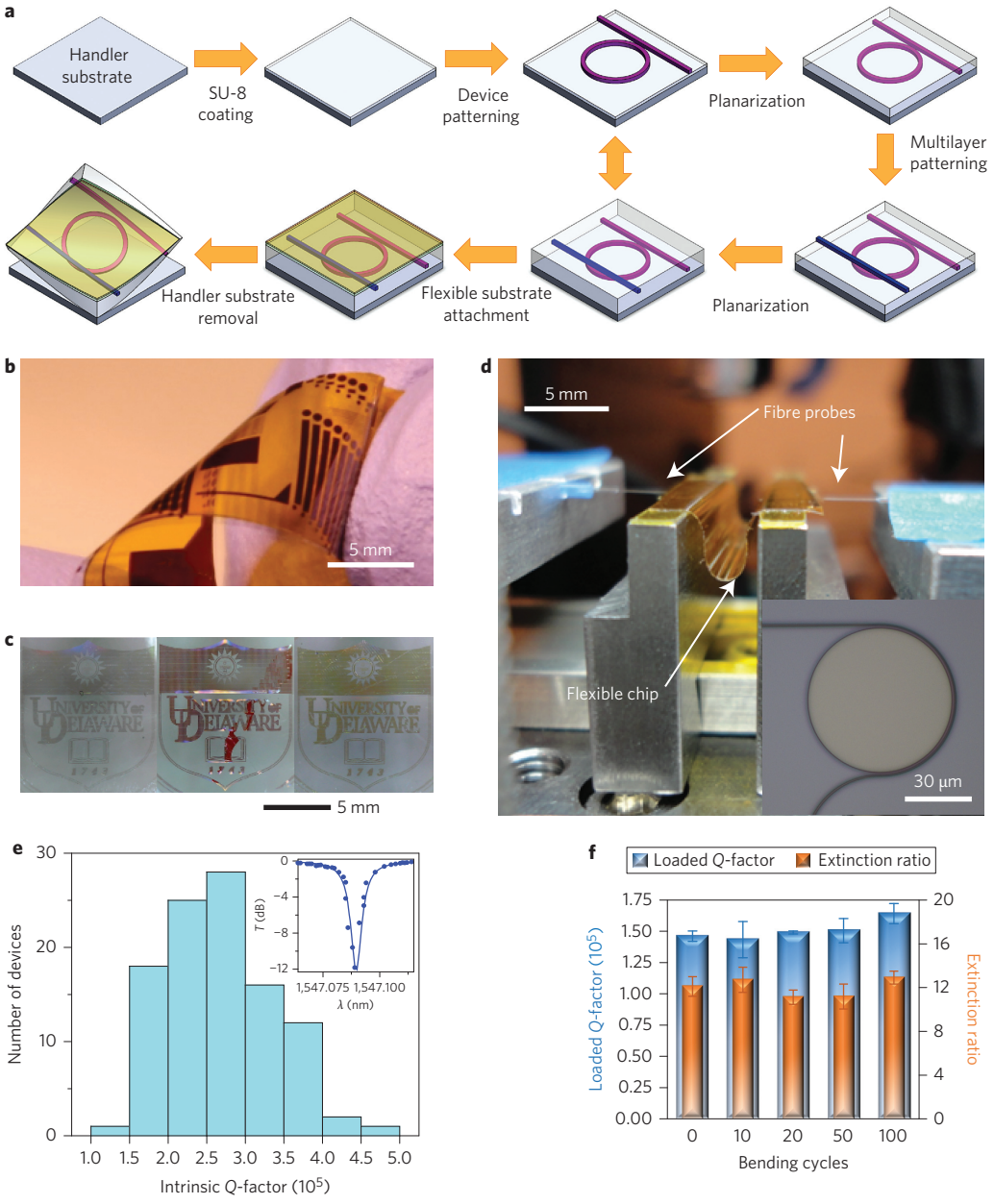

Figure 1 | Flexible glass photonic device fabrication and mechanical reliability tests. a, Schematic overview of the monolithic 3D flexible photonic device fabrication process. **b**, Photograph of a flexible photonic chip showing a linear array of microdisk resonators. **c**, University of Delaware logo on polydimethylsiloxane flexible substrates made of $Ge_{23}Sb_7S_{70}$, As_2Se_3 and As_2S_3 glasses (from left to right). **d**, Photograph of the fibre end-fire testing set-up used for *in situ* measurement of optical transmission characteristics during mechanical bending of the flexible devices. **e**, Intrinsic *Q*-factor distribution measured in flexible microdisk resonators. Inset: example of resonator transmission spectrum. **f**, Loaded *Q*-factors and extinction ratios of the resonator after multiple bending cycles at a bending radius of 0.5 mm.

capture the strain–optical coupling behaviour in our devices. We also further exploited the monolithic integration approach for three-dimensional (3D) multilayer fabrication. Compared to conventional 3D stacking methods involving wafer bonding[17], nanomanipulation[18], ion implantation[19], or multi-step chemical mechanical polishing[20], our approach offers a more simple and robust alternative route for novel 3D photonic structure processing.

Device fabrication and mechanical reliability test

Figure 1a schematically illustrates our device fabrication process flow. The process begins by spin-coating epoxy (SU-8) onto a rigid handler (for example, an oxide coated Si wafer), followed by ChG evaporation deposition and liftoff patterning using ultraviolet contact lithography (see Methods). We chose ChGs as the photonic materials for several reasons, including their amorphous nature and low deposition temperature (allowing direct monolithic flexible substrate integration[21–24]), their high refractive indices (2–3, compatible with high-index-contrast photonic integration), and their almost infinite capacity for composition alloying (allowing fine-tuning of optical as well as thermomechanical properties over a broad range), making them suitable for diverse applications. SU-8 epoxy was used as the cladding polymer because of its proven chemical stability, excellent optical transparency and superior planarization capacity. Before ultraviolet exposure SU-8 epoxy behaves as a thermoplastic polymer amenable to thermal reflow treatments and the creation of a smooth surface finish, even on substrates with

© 2014 Macmillan Publishers Limited. All rights reserved.

multilevel patterned structures. After thermal or ultraviolet cross-linking the epoxy becomes a thermosetting resin and is robust against mechanical deformation, humidity and subsequent thermal processing. Capitalizing on this unique property of SU-8, we developed an ultrathin epoxy planarization process with the high degree of planarization critical to 3D photonic integration. Details of the planarization process are described in Supplementary Section I. The deposition/patterning/planarization steps were repeated multiple times for 3D fabrication and no loss of degree of planarization was observed. Finally, the flexible samples were delaminated from the handler wafer using Kapton tape to form free-standing flexible structures. The Kapton tape consists of two layers, a silicone adhesive layer and a polyimide substrate, and has dual purposes: (1) it facilitates the delamination process and (2) the low-modulus silicone adhesive serves as an effective strain-relieving agent in our local-neutral-axis design (discussed in the following). Figure 1b presents a photograph of a final free-standing flexible photonic circuit chip. We have also tested the fabrication process with several different ChG compositions with vastly different optical properties (indices and Tauc optical bandgaps) to demonstrate the material compatibility of the process. Figure 1c shows University of Delaware logos patterned on flexible substrates with three different glass compositions: $Ge_{23}Sb_7S_{70}$ (n = 2.1, E_g = 2.2 eV)[25], As_2Se_3 (n = 2.8, E_g = 1.8 eV)[26] and As_2S_3 (n = 2.4, E_g = 2.1 eV)[27], all of which exhibit good adhesion to the SU-8 substrate. The inset in Fig. 1d shows a microscope image of a 30-μm-radius and 450-nm-thick $Ge_{23}Sb_7S_{70}$ microdisk resonator pulley coupled to an 800-nm-wide channel bus waveguide[28]. This simple fabrication route offers extremely high device yields; we have tested over 100 resonator devices randomly selected from samples fabricated in several different batches and all of them operated as designed after going through the entire fabrication process. Figure 1e plots the intrinsic Q-factor distribution of the devices measured near a wavelength of 1,550 nm, showing an average Q-factor of $(2.7 \pm 0.7) \times 10^5$, corresponding to an equivalent optical propagation loss of 1.6 ± 0.4 dB cm^{-1} (Supplementary Fig. 2a). An example of a normalized resonator transmission spectrum is shown in the inset to Fig. 1e. Our best device exhibited an intrinsic Q-factor as high as 460,000, the highest value ever reported in photonic devices on plastic substrates.

A schematic illustration of the thickness profile of a fabricated flexible photonic chip is provided in Supplementary Fig. 6a. This photonic chip is composed of (top to bottom) a polyimide substrate, the silicone adhesive and the SU-8 cladding layer in which the devices are encapsulated. The notations are labelled in Supplementary Fig. 6a and tabulated in Supplementary Table 4. We experimentally measured the Young's moduli of the thin-film polyimide, silicone and SU-8 to be E_1 = 2.5 GPa, E_2 = 1.5 MPa and E_3 = 2 GPa, respectively (Supplementary Section IV). In the following we derive an analytical formula to predict the strain–optical coupling behaviour in the devices.

Classical beam bending theory predicts that when a multilayer structure is subject to pure bending, cross-sectional planes before bending are assumed to remain planar after bending and a unique neutral axis exists in the laminated structure (Supplementary Section V). However, the classical theory is only applicable to multilayer stacks where the layers have similar elastic stiffnesses. For the three-layer structure shown in Supplementary Fig. 6a, the Young's modulus of the silicone interlayer is three orders of magnitude smaller than that of the SU-8 or polyimide. When this sandwiched 'Oreo' structure is bent, the soft middle layer undergoes large shear deformation, which essentially decouples the deformation of the top and bottom stiff layers, similar to the strain decoupling effect discussed in the tension case[29]. As a result, each stiff layer has its own neutral axis and bending centre, and the stack thus demonstrates multiple neutral axes. We validated this postulate using both finite-element modelling (FEM) and an analytical multi-neutral axis theory, as discussed in Supplementary Section V. Because of the soft silicone interlayer, the location of the neutral axis can be shifted away from near the centre of the multilayer stack to within SU-8, a salient feature that enables photonic designs capitalizing on and enabling evanescent interactions while demonstrating extraordinary mechanical flexibility.

To experimentally validate the new theory, we performed strain–optical coupling measurements, where the optical resonant wavelengths of glass microdisk resonators were monitored *in situ* while the samples were bent. A block diagram of the home-built measurement set-up is illustrated in Supplementary Fig. 7a. Light from a tunable laser was coupled into the bus waveguides via fibre end-fire coupling, and the transmittance through the chip was monitored *in situ* as the samples were bent using linear motion stages. Figure 1d shows a flexible chip under testing. Further details regarding the measurement are provided in Supplementary Section VI.

The resonant wavelength shift $d\lambda$ can be expressed as a function of the local strain at the resonator, $d\varepsilon$:

$$\frac{d\lambda}{d\varepsilon} = \sum_i \left[\frac{\lambda}{n_g} \cdot \Gamma_i \cdot \left(\frac{dn}{d\varepsilon} \right)_i \right] + \frac{n_{eff}}{n_g} \cdot \frac{\lambda}{L} \cdot \frac{dL}{d\varepsilon} + \frac{\lambda}{n_g} \cdot \frac{dn_{eff}}{d\varepsilon} \qquad (1)$$

where Γ_i and $(dn/d\varepsilon)_i$ are the optical confinement factor and strain–optic coefficient in the ith cavity material, L is the cavity length, and n_g and n_{eff} denote the group and effective indices, respectively. In equation (1), the first term on the right-hand side represents the optoelastic (that is, strain–optic) material response, the second term manifests the cavity length change, and the third term results from the cavity cross-sectional geometry modification. Derivation of the equation follows ref. 11 and is elaborated in Supplementary Section VII. Because the resonant wavelength of a high-Q resonator can be measured accurately down to the picometre level, strain–optical coupling provides a sensitive measure of local strain in the multilayer structure. A series of flexible $Ge_{23}Sb_7S_{70}$ glass microdisk resonator samples with different SU-8 top and bottom cladding layer thickness combinations were fabricated and tested. By varying the cladding thickness, local strain at the microdisk resonators is modified when the samples are bent. This is apparent from Fig. 2a, where the resonant wavelength shift as a function of chip bending curvature is plotted for five different samples. The resonant wavelength shift was highly repeatable after several bending cycles, and little hysteresis was observed. Theoretical predictions based on classical multilayer bending theory as well as those made using our new multi-neutral-axis analysis are plotted in the same figure for comparison. Experimentally measured material moduli and strain–optic coefficients measured using the protocols outlined in Supplementary Section IV were used in the calculations. It is apparent that the classical theory fails to reproduce the experimentally observed trend, whereas our new theory successfully accounts for the strain–optical coupling behaviour. When we apply Supplementary equation (14) to convert the horizontal axis from the bending curvature in Fig. 2a to the bending-induced strain in Fig. 2b, all of the experimental data collapse onto one straight line, which verifies the linear dependence of the resonance peak shift on mechanical strain (equation (1)). The dramatic change of both the magnitude and sign of the resonance shift in different samples provides an effective method to control strain–optical coupling in flexible photonic devices and also has important practical implications. For applications where strain–optical coupling is undesirable, such as resonator refractometry sensing, the coupling can be nullified by strategically placing the device at the zero strain points. On the other hand, the coupling can be maximized when applied to photonic tuning or strain sensing.

© 2014 Macmillan Publishers Limited. All rights reserved.

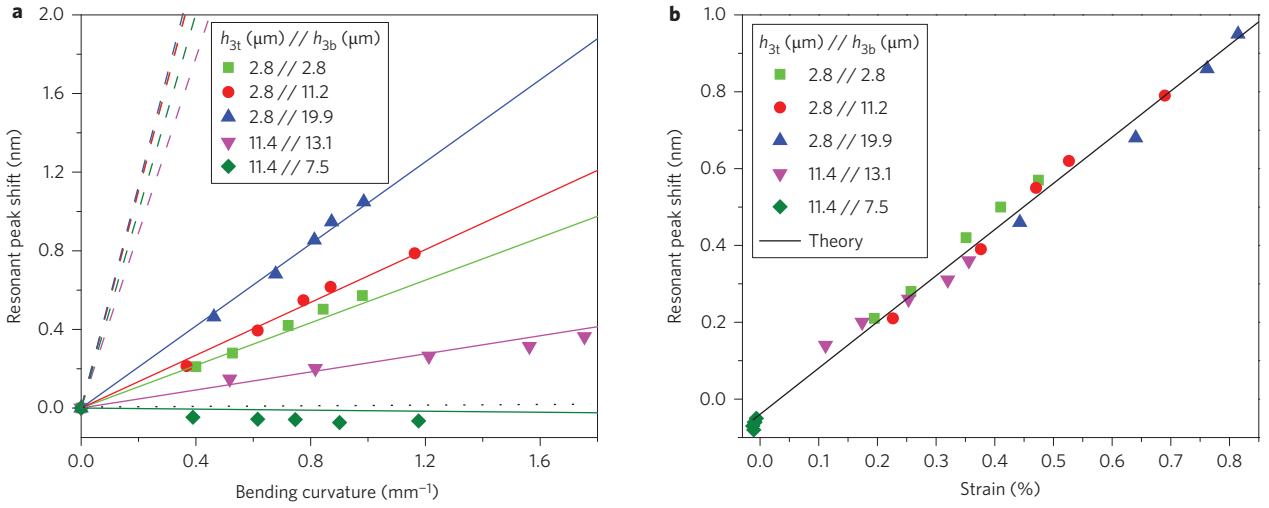

Figure 2 | Strain-optical coupling in flexible photonic devices. a, Resonance wavelength shift plotted as a function of bending curvature: each colour represents an SU-8 top/bottom cladding thickness combination. h_{3t} and h_{3b} denote the SU-8 top and bottom cladding thicknesses, as labelled in Supplementary Fig. 6a. Symbols are experimentally measured data, solid lines are predictions made using our analytical theory, and dashed lines are classical bending theory results. **b**, Resonance wavelength shift plotted as a function of bending strain, which can be calculated from the bending curvature using Supplementary equation (14). All data in Fig. 2b collapse to one curve, as predicted by equation (1).

The local neutral axis design imparts extreme mechanical flexibility to our devices. To test the mechanical reliability of the flexible devices, microdisk resonators were fabricated and their optical characteristics were measured after repeated bending cycles with a bending radius of 0.5 mm. As shown in Fig. 1f, there were minimal variations in both the quality factor and the extinction ratio after multiple bending cycles, demonstrating the superior mechanical robustness of the flexible devices. Our fatigue test, consisting of up to 5,000 bending cycles at a radius of 0.8 mm, resulted in a 0.5 dB cm^{-1} increase in waveguide propagation loss and a 23% decrease in the resonator intrinsic Q-factor (Supplementary Section III). Optical microscopy further revealed no crack formation or interface delamination in the layers after 5,000 bending cycles (Supplementary Fig. 4).

Adiabatic interlayer waveguide couplers

As our technology makes use of high-index ChGs as the backbone photonic materials, their amorphous nature further enables us to scale the fabrication method to 3D monolithic photonic integration on plastic substrates using multilayer deposition and patterning.

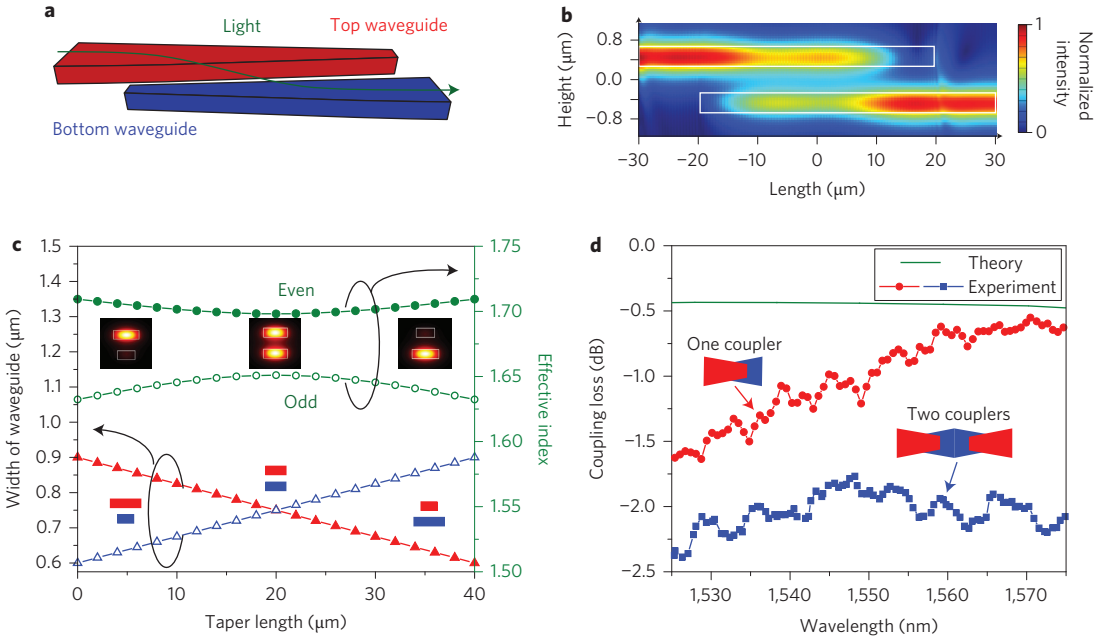

Figure 3 | Adiabatic interlayer waveguide couplers. a, Schematic structure of the interlayer waveguide coupler. **b**, Side view of steady-state optical field intensity distribution in the coupler, showing adiabatic power transfer from the top waveguide to the bottom waveguide. **c**, Top (red curve) and bottom (blue curve) waveguide widths and simulated supermode effective indices (green curves) in the taper section of the interlayer coupler. Insets: cross-sectional even supermode intensity profile evolution along the taper. **d**, FDTD simulated (green line) and measured (red and blue lines) transmission spectra of the interlayer coupler(s).

© 2014 Macmillan Publishers Limited. All rights reserved.

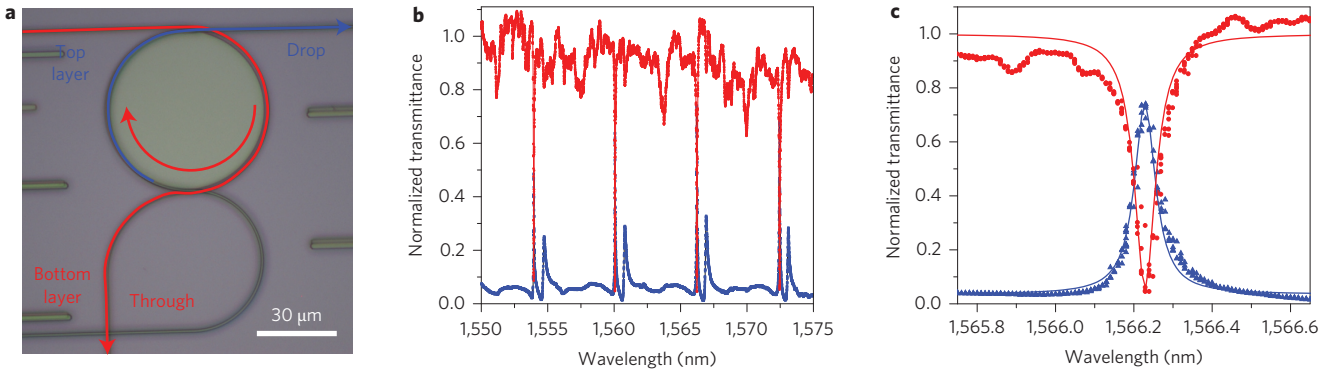

Figure 4 | Vertically coupled add–drop resonator filter. a, Optical microscope image of a two-layer vertically coupled resonator. **b**,**c**, Normalized transmission spectra of a vertically coupled resonator at its through (red) and drop (blue) ports. The device is designed to operate at the critical coupling regime near a wavelength of 1,550 nm. Symbols represent experimental data and lines are theoretical results calculated using a scattering matrix formalism.

The excellent planarization capability of ultrathin SU-8 resin ensures pattern fidelity in the multilayer process. This approach to 3D photonic structure fabrication offers a facile and simple alternative to conventional methods involving ion implantation[19], wafer bonding[17] or pick-and-place nanomanipulation[18]. Here, we demonstrate the fabrication of several important device building blocks, including broadband interlayer waveguide couplers, vertically coupled resonators and woodpile photonic crystals, using our approach. It is worth noting that all devices presented in this Article were fabricated using simple, low-cost ultraviolet contact lithography, without resorting to fine-line patterning tools such as electron-beam lithography or deep-ultraviolet lithography, and we expect significant device performance improvement through further optimization of the processing steps.

Figure 3a schematically shows the structure of an interlayer adiabatic waveguide coupler. The coupler consists of a pair of vertically overlapping inverse taper structures made of $Ge_{23}Sb_7S_{70}$ glass. The non-tapered waveguide sections are 0.9 μm wide and 0.4 μm high, designed for single quasi-transverse-electric mode operation at a wavelength of 1,550 nm. The device operates on the supermode adiabatic transformation principle[30,31], where light entering the coupler predominantly remains in the coupled waveguide system's fundamental mode. The simulated field mode intensity profiles of the coupled waveguides in the taper section are plotted in the insets to Fig. 4c. The effective indices of the even and odd modes were also plotted along the taper length. As shown in the figure, the even supermode, which is the fundamental mode of the coupled waveguide system, transitions adiabatically from the top waveguide to the bottom waveguide as the waveguide width changes in the taper section. Figure 3b shows a side view of the finite-difference time-domain (FDTD) simulated steady-state optical field intensity distribution in the coupler, which illustrates the power transfer process from the top waveguide to the bottom waveguide. Unlike traditional directional couplers based on phase-matched evanescent coupling, the adiabatic mode transformer coupler design is robust against fabrication error and wavelength dispersion. The adiabatic interlayer coupler exhibited broadband operation with 1.1 dB (single coupler) and 2.0 dB (double couplers) insertion loss (both averaged over a 50 nm band), comparable to the simulation results (0.5 dB loss per coupler) given the limited alignment accuracy of contact lithography and the waveguide sidewall roughness scattering loss (Fig. 3d).

Vertically coupled add–drop resonator filter

Vertically coupled resonator add–drop filters were fabricated using the same approach on plastic substrates (Fig. 4a). The device consists of a microdisk resonator co-planar with the add waveguide, and a through-port waveguide in a second layer separated from the microdisk by a 550-nm-thick SU-8 layer. Unlike co-planar add–drop filters where the coupling strength has to be adjusted by changing the narrow gap width between the bus waveguides and the resonator, the critical coupling regime in vertical resonators is readily achieved by fine-tuning the thickness of the SU-8 separation layer. Figure 4c shows the normalized transmission spectrum of a resonator designed for critical coupling operation. The filter exhibited an insertion loss of 1.2 dB and a loaded Q-factor of 2.5×10^4 at both its through port and its drop port. These results agree well with our theoretical predictions made using a scattering matrix formalism[32] (Supplementary Section IX).

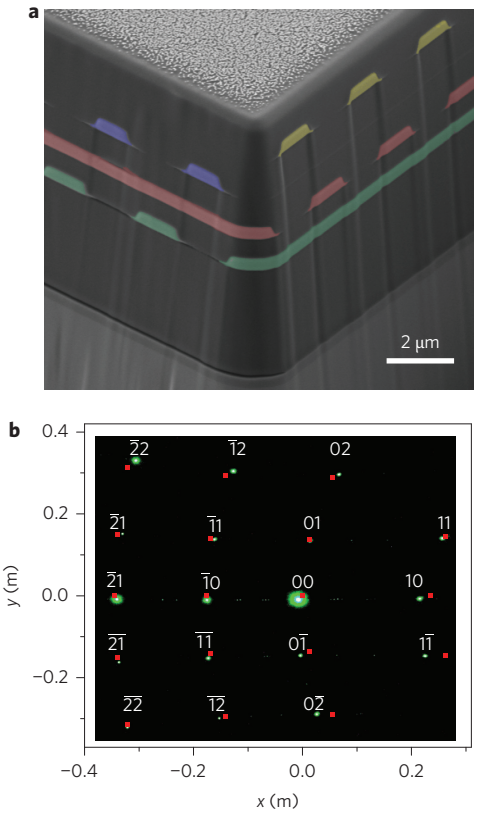

Figure 5 | 3D woodpile photonic crystals. a, Tilted focused ion beam-scanning electron microscopy view of a 3D woodpile photonic crystal (before delamination from the silicon handler substrate) showing excellent structural integrity. **b**, Diffraction patterns of a collimated 532 nm green laser beam from the photonic crystal. Red dots are diffraction patterns simulated using the Bragg diffraction equation.

3D woodpile photonic crystals

In addition to being used to fabricate two-layer devices such as interlayer couplers and vertically coupled resonator filters, our technique can be readily extended to the fabrication of multilayer structures that often present major challenges to conventional fabrication methods. As an example, Fig. 5a shows a tilted anatomy view of a four-layer woodpile photonic crystal fabricated using the method shown in Fig. 1a, before delamination from the handler substrate. The integrity and pattern fidelity of the photonic crystal structure were examined using optical diffraction. Figure 5b shows the diffraction spots from a collimated 532 nm green laser beam. The red dots in Fig. 5b represent the diffraction pattern calculated using Bragg equations (calculation details are presented in Supplementary Section IX), which matches nicely with the experimental results. The well-defined diffraction pattern indicates excellent long-range structural order of the photonic crystal.

In conclusion, we have experimentally demonstrated a simple and versatile method to fabricate high-index-contrast 3D photonic devices on flexible substrates. The method leverages the amorphous nature and low deposition temperature of novel ChG alloys to pioneer a 3D multilayer monolithic integration approach with dramatically improved device performance, processing throughput and yield. A new mechanical theory was developed and experimentally validated to accurately predict and control the strain–optical coupling mechanisms in the device. Guided by the multi-neutral axis theory, we have demonstrated mechanically robust devices with extreme flexibility, despite the inherent mechanical fragility of the glass film, and the devices can be twisted and bent to sub-millimetre radii without compromising their optical performance. The 3D monolithic integration technique, which is applicable to photonic integration on both traditional rigid substrates and non-conventional plastic substrates, is expected to open up new application venues such as high-bandwidth-density optical interconnects[33], conformal wearable sensors and ultrasensitive strain gauges.

Methods

Material and device fabrication. Device fabrication was carried out at the University of Delaware Nanofabrication Facility. An SU-8 epoxy layer was first spin-coated onto the handler wafer, and a negative photoresist (NR9-1000PY, Futurrex) pattern was then lithographically defined on the SU-8 layer using contact lithography on an ABM Mask Aligner. ChG films were thermally evaporated onto the substrates from bulk glasses synthesized using a melt-quenching technique. Deposition was performed using a custom-designed system (PVD Products). The deposition rate was monitored in real time using a quartz crystal microbalance and was stabilized at 20 Å s^{-1}. After deposition, the sample was sonicated in acetone to dissolve the resist layer, leaving a glass pattern the reverse of the photoresist. The procedure was repeated several times to fabricate 3D structures. The fabricated glass devices were flood-exposed using a halogen lamp before optical testing to nullify the glass film's photosensitivity.

Finite-element simulations. Finite-element simulations were applied by ABAQUS 6.10 using plane strain elements (CPE4R) for the multilayer structure. In the experiment, the concave bending of the polyimide–silicone–SU-8 three-layer structure was induced through the buckling mode (Fig. 1d) instead of pure bending. With this concave bending the polyimide layer, which has a larger bending rigidity than the other two layers, is subject to the largest part of the bending moment, so the bending of the other two layers can be considered as being forced by the polyimide layer. To simulate this buckling-induced bending we applied rotation boundary conditions on the two ends of the polyimide layer, thereby generating curvatures the same as in the experiments at the middle point of the structure.

Optical transmission measurements. The optical transmission spectra of waveguides and resonators in the C and L bands were collected using a fibre end-fire coupling approach as shown in Supplementary Fig. 7a. Tapered lens-tip fibres were used to couple light from an external cavity tunable laser (Agilent 81682A) into and out of the waveguides through end facets formed by cleaving the samples before delamination from the silicon handler substrates. Supplementary Fig. 7b presents a far-field image of a quasi-transverse-electric guided mode output from a single-mode $Ge_{23}Sb_7S_{70}$ glass waveguide.

Received 26 July 2013; accepted 27 May 2014;
published online 29 June 2014

References

1. Ko, H. C. *et al.* A hemispherical electronic eye camera based on compressible silicon optoelectronics. *Nature* **454,** 748–753 (2008).
2. Kim, D.-H. *et al.* Epidermal electronics. *Science* **333,** 838–843 (2011).
3. Bosman, E. *et al.* Highly reliable flexible active optical links. *IEEE Photon. Technol. Lett.* **22,** 287–289 (2010).
4. Chen, Y., Li, H. & Li, M. Flexible and tunable silicon photonic circuits on plastic substrates. *Sci. Rep.* **2,** 622 (2012).
5. Yang, W. *et al.* Large-area InP-based crystalline nanomembrane flexible photodetectors. *Appl. Phys. Lett.* **96,** 121107 (2010).
6. Park, S.-I. *et al.* Printed assemblies of inorganic light-emitting diodes for deformable and semitransparent displays. *Science* **325,** 977–981 (2009).
7. Zhou, W. *et al.* Flexible photonic-crystal Fano filters based on transferred semiconductor nanomembranes. *J. Phys. D* **42,** 234007 (2009).
8. Xu, X. *et al.* Stamp printing of silicon-nanomembrane-based photonic devices onto flexible substrates with a suspended configuration. *Opt. Lett.* **37,** 1020–1022 (2012).
9. Ma, Z. *et al.* Fast flexible electronics based on printable thin mono-crystalline silicon. *ECS Trans.* **34,** 137–142 (2011).
10. Zablocki, M. J., Sharkawy, A., Ebil, O. & Prather, D. W. Nanomembrane transfer process for intricate photonic device applications. *Opt. Lett.* **36,** 58–60 (2011).
11. Fan, L. *et al.* Direct fabrication of silicon photonic devices on a flexible platform and its application for strain sensing. *Opt. Express* **20,** 20564–20575 (2012).
12. Bauters, J. F. *et al.* Ultra-low-loss high-aspect-ratio Si_3N_4 waveguides. *Opt. Express* **19,** 3163–3174 (2011).
13. Sandland, J. G. *Sputtered Silicon Oxynitride for Microphotonics: A Materials Study.* PhD thesis, Massachusetts Institute of Technology (2005).
14. Jaeyoun, K., Winick, K. A., Florea, C. & McCoy, M. Design and fabrication of low-loss hydrogenated amorphous silicon overlay DBR for glass waveguide devices. *IEEE J. Sel. Top. Quantum Electron.* **8,** 1307–1315 (2002).
15. Ma, Z. An electronic second skin. *Science* **333,** 830–831 (2011).
16. Kim, D.-H. *et al.* Stretchable and foldable silicon integrated circuits. *Science* **320,** 507–511 (2008).
17. Ishizaki, K., Koumura, M., Suzuki, K., Gondaira, K. & Noda, S. Realization of three-dimensional guiding of photons in photonic crystals. *Nature Photon.* **7,** 133–137 (2013).
18. Aoki, K. *et al.* Microassembly of semiconductor three-dimensional photonic crystals. *Nature Mater.* **2,** 117–121 (2003).
19. Koonath, P. & Jalali, B. Multilayer 3-D photonics in silicon. *Opt. Express* **15,** 12686–12691 (2007).
20. Sherwood-Droz, N. & Lipson, M. Scalable 3D dense integration of photonics on bulk silicon. *Opt. Express* **19,** 17758–17765 (2011).
21. Carlie, N. *et al.* Integrated chalcogenide waveguide resonators for mid-IR sensing: leveraging material properties to meet fabrication challenges. *Opt. Express* **18,** 26728–26743 (2010).
22. Hu, J. *et al.* Optical loss reduction in high-index-contrast chalcogenide glass waveguides via thermal reflow. *Opt. Express* **18,** 1469–1478 (2010).
23. DeCorby, R. G., Ponnampalam, N., Nguyen, H. T. & Clement, T. J. Robust and flexible free-standing all-dielectric omnidirectional reflectors. *Adv. Mater.* **19,** 193–196 (2007).
24. Abouraddy, A. F. *et al.* Towards multimaterial multifunctional fibres that see, hear, sense and communicate. *Nature Mater.* **6,** 336–347 (2007).
25. Petit, L. *et al.* Correlation between physical, optical and structural properties of sulfide glasses in the system Ge–Sb–S. *Mater. Chem. Phys.* **97,** 64–70 (2006).
26. Chauhan, R., Srivastava, A. K., Tripathi, A. & Srivastava, K. K. Linear and nonlinear optical changes in amorphous As_2Se_3 thin film upon UV exposure. *Prog. Nat. Sci. Mater. Int.* **21,** 205–210 (2011).
27. Ruan, Y., Jarvis, R. A., Rode, A. V., Madden, S. & Luther-Davies, B. Wavelength dispersion of Verdet constants in chalcogenide glasses for magneto-optical waveguide devices. *Opt. Commun.* **252,** 39–45 (2005).
28. Hu, J. *et al.* Planar waveguide-coupled, high-index-contrast, high-*Q* resonators in chalcogenide glass for sensing. *Opt. Lett.* **33,** 2500–2502 (2008).
29. Sun, J.-Y. *et al.* Inorganic islands on a highly stretchable polyimide substrate. *J. Mater. Res.* **24,** 3338–3342 (2009).
30. Yariv, A. in *Optical Electronics in Modern Communications* 526–531 (Oxford Univ. Press, 1997).
31. Sun, R. *et al.* Impedance matching vertical optical waveguide couplers for dense high index contrast circuits. *Opt. Express* **16,** 11682–11690 (2008).
32. Schwelb, O. Transmission, group delay, and dispersion in single-ring optical resonators and add/drop filters—a tutorial overview. *J. Lightwave Technol.* **22,** 1380–1394 (2004).
33. Li, L. *et al.* A fully-integrated flexible photonic platform for chip-to-chip optical interconnects. *J. Lightwave Technol.* **31,** 4080–4086 (2013).

Acknowledgements

The authors thank S. Kozacik, M. Murakowski and D. Prather for assistance with device fabrication, N. Nguyen and M. Mackay for mechanical tests, N. Xiao and Y. Liu for assistance with optical measurement data processing, V. Singh for help with FIMMWAVE simulations and T. Gu and M. Haney for helpful discussions. L.L. acknowledges funding

support from Delaware NASA/EPSCoR through a Research Infrastructure Development (RID) grant. H.L. and J.H. acknowledge funding support from the National Science Foundation (award no. 1200406). N.L. acknowledges start-up funding support from the Cockrell School of Engineering of the University of Texas, Austin. This work is based upon work supported in part by the National Science Foundation under cooperative agreement no. EEC-1160494. Any opinions, findings and conclusions or recommendations expressed in this material are those of the author(s) and do not necessarily reflect the views of the National Science Foundation.

Author contributions

L.L. and H.L. conducted material synthesis, optical modelling, device fabrication and testing. S.Q. and N.L. performed mechanics modelling and analysis. Y.Z. assisted with film deposition and device characterization. J.H. conceived the device and structural designs. S. D., J.D.M. and K.R. contributed to material synthesis. J.H., N.L. and K.R. supervised and coordinated the project. All authors contributed to writing the paper.

Additional information

Supplementary information is available in the online version of the paper. Reprints and permissions information is available online at www.nature.com/reprints. Correspondence and requests for materials should be addressed to J.H.

Competing financial interests

The authors declare no competing financial interests.

nature photonics

SUPPLEMENTARY INFORMATION

DOI: 10.1038/NPHOTON.2014.138

Supplementary Information

Integrated flexible chalcogenide glass photonic devices

Lan Li[1†], Hongtao Lin[1†], Shutao Qiao[2†], Yi Zou[1], Sylvain Danto[3], Kathleen Richardson[3, 4], J. David Musgraves[4], Nanshu Lu[2], and Juejun Hu[1*]

1. Department of Materials Science and Engineering

University of Delaware

Newark, Delaware 19716

2. Centre for Mechanics of Solids, Structures and Materials

Department of Aerospace Engineering and Engineering Mechanics

University of Texas at Austin

Austin, Texas 78712

3. College of Optics and Photonics, CREOL

Department of Materials Science and Engineering

University of Central Florida

Orlando, Florida 32816

4. IRradiance Glass Inc.

Orlando, FL 32828, USA

†These authors contributed equally to this work.

*e-mail: hujuejun@udel.edu

© 2014 Macmillan Publishers Limited. All rights reserved.

DOI: 10.1038/NPHOTON.2014.138

In this Supplementary Information, we provide further details on the device fabrication, characterization, and simulation results.

I. Ultra-thin SU-8 planarization tests

II. Propagating loss in $Ge_{23}Sb_7S_{70}$ glass micro-resonators fabricated on flexible substrates and the impact of bending

III. Fatigue test on flexible photonic devices

IV. Measurements of material mechanical and optical properties

V. FEM simulation and analytical modeling accounting for multiple neutral axes in the multilayer stack

VI. *In-situ* strain-optical coupling characterization method

VII. Strain-optical coupling theory

VIII. Optimized 3-D photonic device design parameters

IX. Scattering matrix formalism for calculating the transfer function of vertically coupled add-drop filters

X. Woodpile photonic crystal diffraction experiment configuration

© 2014 Macmillan Publishers Limited. All rights reserved.

I. Ultra-thin SU-8 planarization tests

Planarization is the key to our multilayer 3-D fabrication process. We choose SU-8, an epoxy-based negative photoresist, as the planarizing agent. Unexposed SU-8 is a thermoplastic with a glass transition temperature (T_g) of 50 °C [1], which is amenable to thermal reflow processing at a relatively low temperature to create a smooth surface finish through the action of surface tension. Once cured or UV cross-linked, SU-8 transforms to a thermosetting polymer with a high T_g > 200 °C and stable thermal/mechanical/chemical properties. To validate the planarization behaviour of SU-8 on glass devices, a layer of 460 nm thick SU-8 epoxy was spin coated on gratings patterned in a 360 nm thick $Ge_{23}Sb_7S_{70}$ film (i.e. 100 nm overcoating layer thickness). Fig. S1a shows top-view optical micrographs of the grating patterns after SU-8 spin coating. The gratings have a fixed duty cycle of 0.5 and their periods are varied from 1.2 μm to 120 μm. The SU-8 layer topography after heat treatment was examined using cross-sectional SEM, and Fig. S1b (bottom) shows an exemplary SEM image of the grating structure after planarization. Transfer function of the planarization process was plotted as a function of spatial frequency (reciprocal of grating pitch) in Fig. S1c. Top panel of Fig. S1b schematically illustrated the definition of degree of planarization (DOP) and planarization angle (θ). The degree of planarization (DOP) is given by: $DOP = 100\% * \frac{t_1 - t_2}{t_2}$, and the planarization angle (θ) by $\theta = \arctan(\frac{t_1 - t_2}{W})$, where W is width of the grating line (i.e. half of the grating pitch). The ultra-thin (100 nm thickness) SU-8 overcoating layer produces DOP consistently larger than 98% for patterns with micron-sized pitch. Such planarization performance is considerably better than previous reports using BCB, PMMA or polyimide as the planarization agent, as shown by the comparison in Table S1.

© 2014 Macmillan Publishers Limited. All rights reserved.

DOI: 10.1038/NPHOTON.2014.138

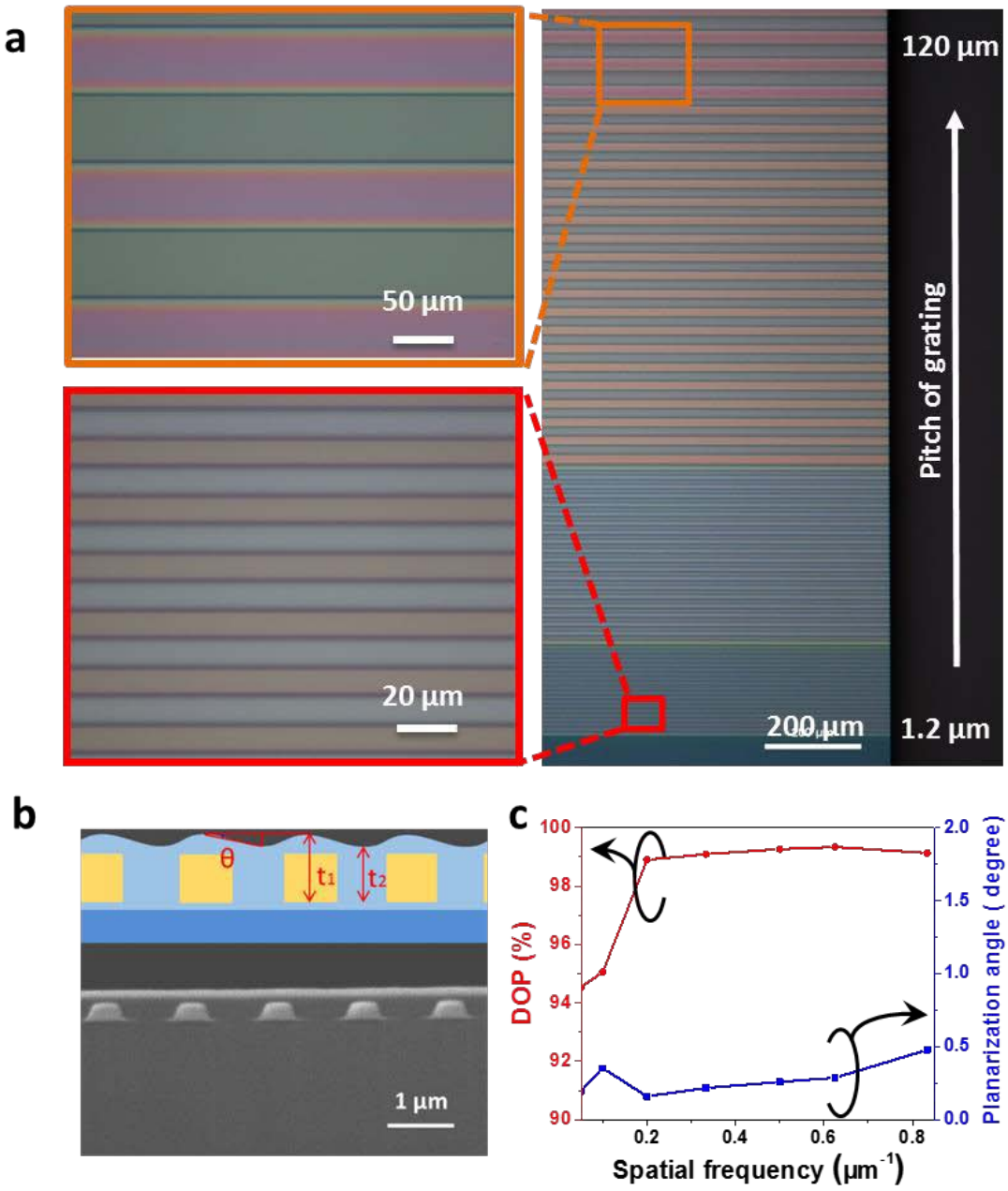

Figure S1 | Ultra-thin SU-8 planarization characterizations. **a**, Optical microscope images of glass grating patterns after single-layer SU-8 planarization. **b**, SEM cross-sectional image of planarized gratings; the top inset illustrates the definition of DOP and planarization angle. **c**, Plot of degree of planarization and planarization angle as functions of spatial frequency. The SU-8 planarization process consistently shows a DOP above 98% over micron-sized features and a small planarization angle < 1°.

© 2014 Macmillan Publishers Limited. All rights reserved.

Table S1 | Degree of planarization (DOP) of thin SU-8 compared to literature values using Polybenzocyclobutene (PBCB), Poly(methyl methacrylate) (PMMA) and polyimide (PI). The overcoating layer thickness is defined as the thickness of the planarization coating minus that of the underlying features to be planarized.

Materials	Overcoating thickness (μm)	Planarized topography	DOP
SU-8 (this report)	0.1	5 μm pitch grating (duty cycle 0.5)	99%
	0.1	20 μm pitch grating (duty cycle 0.5)	95%
BCB[2]	0.3	10 μm wide trenches on a pitch of 30 μm	90%
	0.3	10 μm wide trenches on a pitch of 120 μm	70%
PBCB[3]	4.5	20 μm pitch grating (duty cycle 0.5)	85%
PI2555[3]	1	20 μm pitch grating (duty cycle 0.5)	50%
PMMA[3]	0.5	20 μm pitch grating (duty cycle 0.5)	18%

© 2014 Macmillan Publishers Limited. All rights reserved.

DOI: 10.1038/NPHOTON.2014.138

II. Propagating loss in $Ge_{23}Sb_7S_{70}$ glass micro-resonators fabricated on flexible substrates and the impact of bending

Since the flexible substrates are not amenable to cleavage, it is difficult to use the cut-back method to measure waveguide propagating loss. The non-planar nature of the devices also makes scattered light streak imaging unreliable. Therefore, we choose to evaluate the propagation loss in the flexible photonic devices using optical resonator measurements. The linear propagation loss α in a traveling-wave optical resonator is related to its intrinsic Q-factor Q_{in} through:

$$\alpha = 2\pi n_g / Q_{in}\lambda \quad \text{(S1)}$$

where n_g denotes the group index of the resonant mode and λ is the resonant wavelength. The intrinsic quality factor can be deduced from the loaded Q-factor and resonant peak extinction ratio following protocols outlined in literature[4]. This method is particular suitable for flexible device characterization as it directly probes the modal attenuation in resonators and does not require reproducible facet quality. It is worth noting that since we used micro-disk resonators in our experiments, the loss figures cited in this section refer to the linear propagation loss of micro-disk modes.

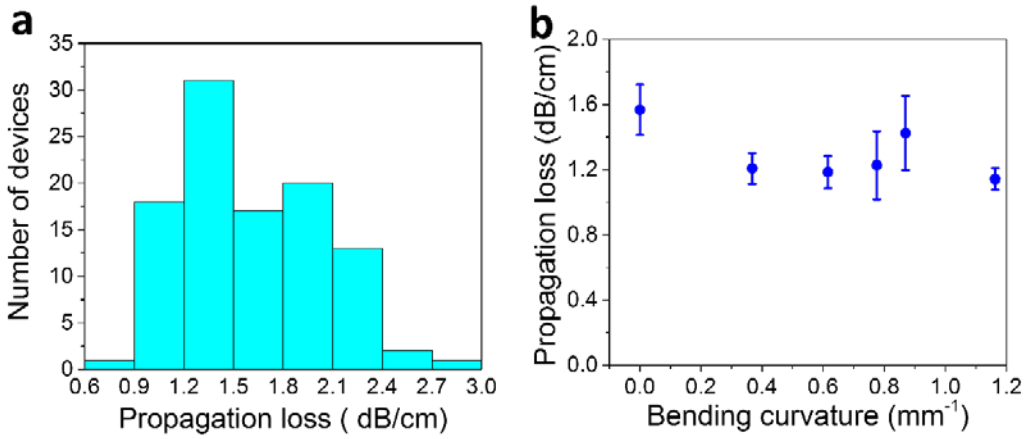

Figure S2 | Propagation loss in flexible optical resonators. **a**, Optical loss distribution measured in flexible micro-disk resonators. **b**, Optical loss in a flexible resonator as a function of bending radius measured when the device was in the mechanically deformed state.

The statistical distribution of propagation loss in the resonator devices we measured is presented in Fig. S2a (calculated from Fig. 1e). The average loss is (1.6 ± 0.4) dB/cm. Our prior

© 2014 Macmillan Publishers Limited. All rights reserved.

measurement showed that the intrinsic material loss in thermally evaporated $Ge_{23}Sb_7S_{70}$ films was well below 0.5 dB/cm[5], and thus sidewall roughness scattering is the primary loss mechanism in our devices. We further note that optical loss in the devices is largely independent of the bending radius when they are mechanically deformed: as an example, Fig. S2b plots the propagation loss in a flexible resonator measured when the device was bent. The change imparted by the bending deformation is insignificant considering the measurement error. This observation can be readily explained by the tight optical confinement in our high-index-contrast photonic devices, which effectively suppresses radiative loss in bent guided wave structures. Fig. S3b shows the quasi-TE mode radiative loss due to bending in a $Ge_{23}Sb_7S_{70}$ waveguide of 800 nm width and 450 nm height, simulated using the full-vectorial waveguide mode solver package FIMMWAVE (Photon Design). It is apparent that radiative bending loss remains negligible down to 50 μm radius. Therefore, it is anticipated that no radiative loss was experimentally observed when we mechanically deform our flexible chip.

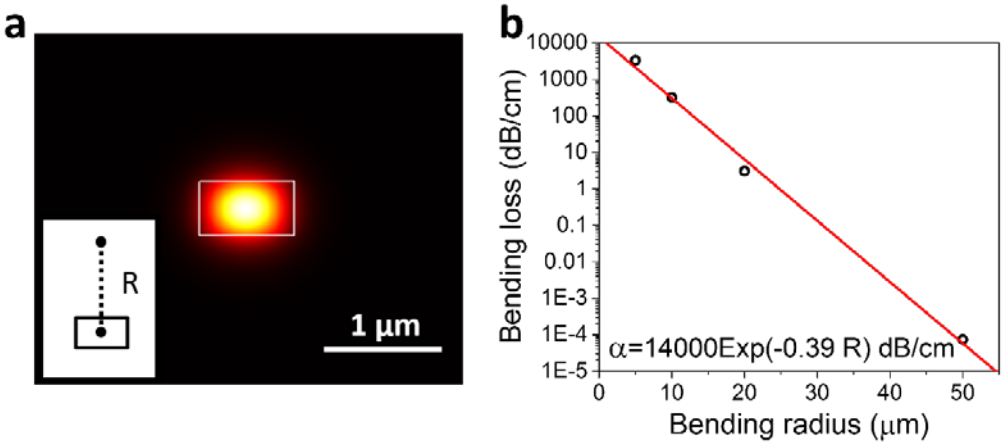

Figure S3 | Bending loss simulations. **a,** Quasi-TE mode intensity profile for a 0.8 μm × 0.45 μm waveguide with a bending radius of 500 μm; the inset illustrates the waveguide bending direction in our mechanical tests. **b**, Radiative bending losses at different bending radii fitted to an exponential model.

© 2014 Macmillan Publishers Limited. All rights reserved.

DOI: 10.1038/NPHOTON.2014.138

III. Fatigue test on flexible photonic devices

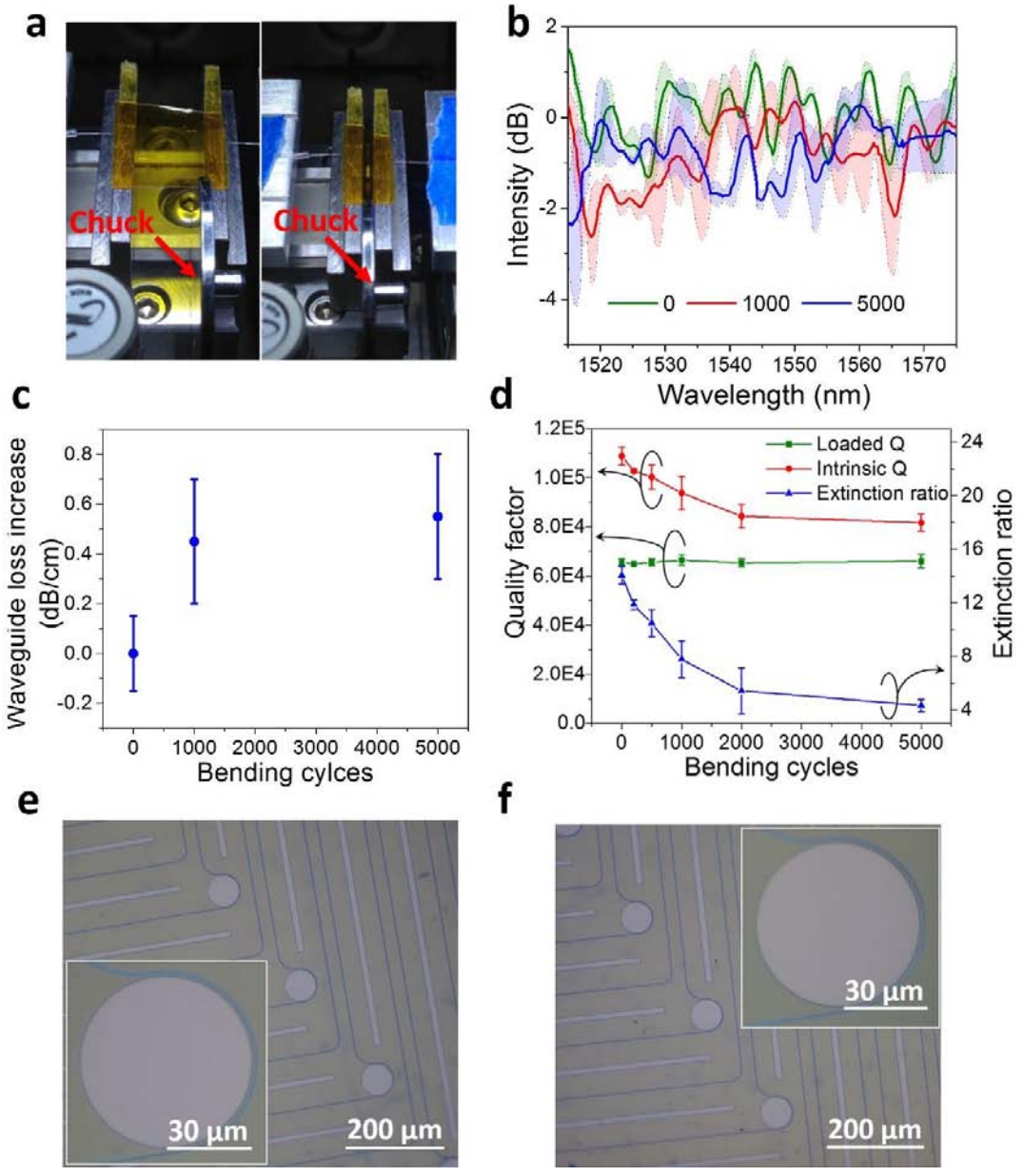

Figure S4 | Fatigue test of the flexible photonic chip. **a**, Photos of the fatigue testing setup. The red arrow points to the metal chuck spacer. **b**, Normalized optical transmission spectra of a flexible waveguide after multiple bending cycles at 0.8 mm bending radius. The shaded regions denote the measurement error bar, which was defined as the standard deviation of optical transmittance collected in multiple transmission measurements. **c**, Spectrum-averaged (1510-1580 nm wavelengths) waveguide propagation loss change due to repeated bending cycles. **d**, Loaded Q-factors, intrinsic Q-factors and extinction ratios of a flexible $Ge_{23}Sb_7S_{70}$ micro-disk

© 2014 Macmillan Publishers Limited. All rights reserved.

resonator after multiple bending cycles at 0.8 mm bending radius. **e**, Top-view optical microscope image of flexible resonators prior to the fatigue test. **f**, Optical microscope image of the same set of resonators after 5,000 bending cycles at 0.8 mm bending radius, revealing structural integrity of the devices free of cracks. The scattered spots are dust particles deposited on the chip surface during the mechanical tests, which were carried out in a non-cleanroom environment.

Fatigue tests of flexible electronic or optoelectronic devices evaluate the mechanical durability of the devices as they undergo repetitive bending for a large number (> 1,000) of cycles. Fig. S4a shows the experimental setup we used for the fatigue test. Two edges of a flexible chip was attached to two sample holders, and the holders were mounted on a sliding track. Linear translational motion of the holders thus resulted in bending of the chip. To reproducibly control the bending radius, metal chucks of different thicknesses were glued to one of the holders as spacers to define the translational distance and hence bending radius. Optical transmission spectra of waveguides and resonators were repeatedly measured in a "flat" state of the chip using fiber end-fire coupling before and after multiple bending cycles at 0.8 mm bending radius. It is worth pointing out that the flexible chip we used for the fatigue tests was a different one from the sample used to obtain the data in Fig. 1f.

Fig. S4b plots the insertion loss of a flexible $Ge_{23}Sb_7S_{70}$ waveguide before and after up to 5,000 bending cycles: the same waveguide was used throughout the measurement to ensure consistent facet quality. The intensity fluctuations were partially attributed to excitation of higher order modes at the 2 μm wide input/output waveguide taper sections. The changes of waveguide propagation loss deduced from the measurement were plotted in Fig. S4c. The results indicate a (0.5 ± 0.3) dB/cm waveguide loss increase after 5,000 cycles at a frequency of 1.5 Hz. The same fatigue tests were performed on $Ge_{23}Sb_7S_{70}$ micro-disk resonators. After 5,000 bending cycles, we observed a 23% decrease of the device intrinsic Q-factor. We inspected the flexible chip under optical microscope (up to 50x magnification) before and after 5,000 bending cycles and no micro-cracks were observed across the chip. Therefore, we conclude that the loss increase (~ 0.5 dB/cm) likely stems from layer delamination or sub-micron cracks that cannot be resolved with an optical microscope, although further study is required to elucidate the loss mechanism. The superior mechanical durability of our devices can be seen from a comparison with state-of-the-art flexible

© 2014 Macmillan Publishers Limited. All rights reserved.

DOI: 10.1038/NPHOTON.2014.138

electronic devices shown in Table S2. To the best of our knowledge, our study also represents the first report of fatigue analysis on flexible micro-electronic or micro-photonic devices that can sustain sub-millimetre bending.

Table S2 | Summary of reported fatigue testing results of flexible micro-electronic and photonic devices.

Device type	Bending radius (mm)	Bending cycles	Performance metric	Percentage change after tests
Chalcogenide glass resonator (this report)	0.8	5000	Quality factor	23%
OLED with transparent contacts[1]	10.5	1000	Electroluminesence intensity	50%
PDMS flat-panel solar cell concentrator[2]	20	1000	Efficiency	Insignificant
Flexible molecular-scale electronics[3]	5	1000	Decay coefficient	17%
Flexible a-IGZO TFT amplifier[4]	5	1000	Gain	Insignificant
Flexible grapheme based capacitor[5]	5	10000	Capacitance	3.5%
Flexible silicon thin film transistor[6]	3	2000	Threshold voltage	< 20%

© 2014 Macmillan Publishers Limited. All rights reserved.

IV. Measurements of material mechanical and optical properties

The Young's moduli of the constituent materials were experimentally extracted from uniaxial tensile tests performed on an RSA3 dynamic mechanical analyser (TA instruments) with a Hencky strain rate of 0.01 s^{-1}. The layer thicknesses were measured by optical microscopy (Fig. S5a). The uniaxial strain-stress characteristics of the silicone adhesive layer and the polyimide layer were measured on the Kapton tapes. Specifically, two sets of experiments were performed: a double-layer Kapton tape was stretched in-plane to determine the modulus of polyimide, and a stack of Kapton tapes (Fig. S5a) underwent out-of-plane tensile tests to extract the strain-stress behaviour of the silicone adhesive layer. In the former case, since the modulus of polyimide is over three orders of magnitude higher than that of silicone, the in-plane stress is pre-dominantly sustained by the polyimide layer. In the latter case, the strain primarily occurred in the silicone layer given its much lower modulus. The two measurements are analogous to the parallel and series connection of two elastic springs with vastly different spring constants (inset of Fig. S5a). Both types of experiments were repeated on multiple (> 6) samples for statistical averaging. The statistically averaged strain-stress curves of polyimide and silicone calculated from the measurement results are plotted in Fig. S5b-c.

In addition to elastic moduli, the strain-optical coefficients are also essential parameters for calculating the strain-optical coupling strength in the flexible resonators, as suggested by Eq. 1. However, measuring strain-optical coefficients, in particular those of thin films (which can be significantly different from those of bulk amorphous glasses), was regarded as extremely challenging task. Here we leverage the flexible resonator devices as a new measurement platform for accurate quantification of strain-optical coefficients of thin film materials. For resonators made of the same material and of the identical dimensions, Eq. 1 suggests the same $d\lambda/d\varepsilon$ coefficient regardless of the flexible device configuration. This conclusion is supported by our experimental results: if we re-plot the strain-induced resonant wavelength shift data (Fig. 2a) as a function of local strain at the resonators, it is clear that all data points fall on a single straight line (Fig. 2b), indicating the same $d\lambda/d\varepsilon$ coefficient (i.e. slope of the line). Since the second and third terms in Eq. 1 (resonator geometry change) can be readily inferred from mechanical simulations, the material strain-optical response can be calculated by subtracting the contributions from the two terms. The calculation was used to generate the theoretical results in Fig. 2a.

© 2014 Macmillan Publishers Limited. All rights reserved.

DOI: 10.1038/NPHOTON.2014.138

Table S3 | Materials parameters used in our FEM simulations

Materials	Young's Modulus (MPa)	Density (g/cc)	Poisson ratio
Polyimide	Fig. S3b	1.42	0.34
Silicone	Fig. S3c	0.97	0.49
SU-8	2000	1.12	0.22

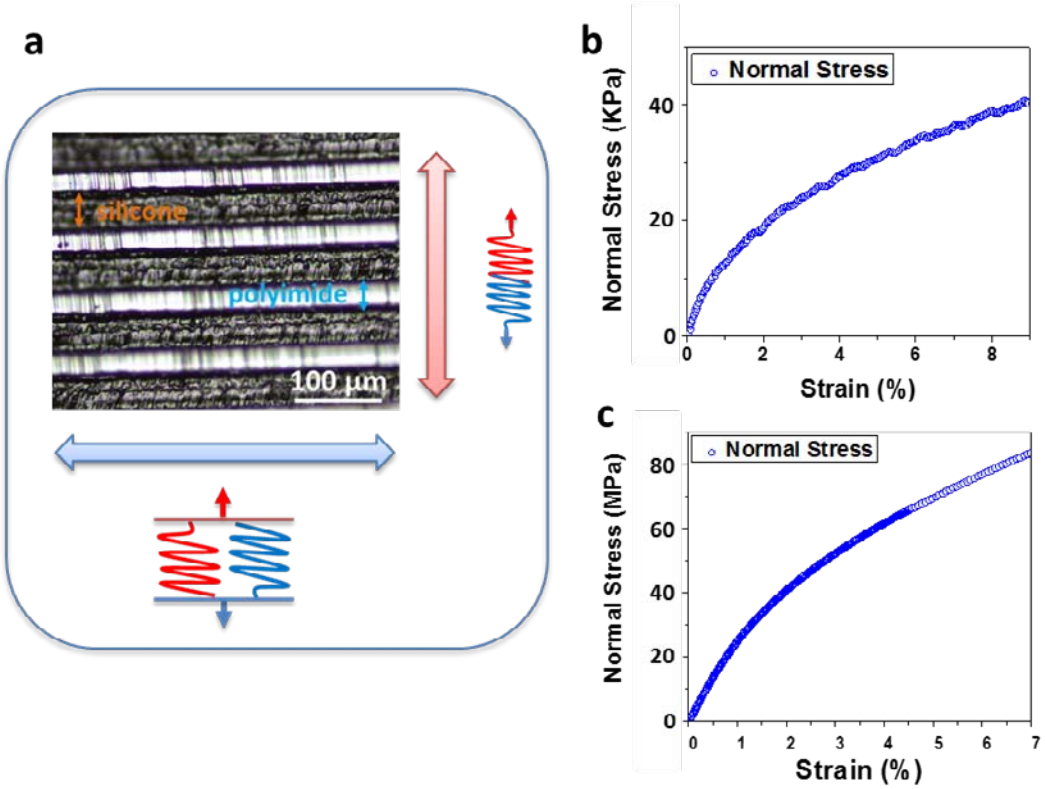

Figure S5 | Mechanical tests of materials used in the flexible photonic device fabrication. a, Cross-sectional optical microscope image of a Kapton tape stack. **b**, Typical stress-strain curve of the silicone layer. **c**, Typical stress-strain curve of the polyimide layer.

© 2014 Macmillan Publishers Limited. All rights reserved.

V. FEM simulation and analytical modelling accounting for multiple neutral axes in the multilayer stack

When a multilayer structure is subject to pure bending, cross-sectional planes before bending are assumed to remain planar after bending in the classical bending theory. Under this assumption, a unique neutral axis of the laminated structure characterized by the distance *b* from the top surface of PI can be written as:

$$b = \frac{\sum_{i=1}^{3} \overline{E}_i h_i \left[\left(\sum_{j=1}^{i} h_j \right) - \frac{h_i}{2} \right]}{\sum_{i=1}^{3} \overline{E}_i h_i} \tag{S2}$$

where $\overline{E}_i = E_i / \left(1 - \nu_i^2\right)$ represents the plane strain Young's modulus with ν_i being the Poisson's ratio. Bending-induced tensile strain can be calculated analytically using:

$$\varepsilon = \frac{y}{\rho} \tag{S3}$$

where *y* is the distance from the point of interest to the neutral axis and ρ represents the radius of the neutral axis. Strain along the neutral axis is exactly zero and strains on different sides of the neutral axis have opposite signs.

Eq. S2 is only applicable to multilayer stacks with similar elastic stiffness. In our design, the PI and SU-8 layers are much stiffer than the silicon adhesive layer and thus Eq. S2 no longer applies. Fig. S6b shows the strain distribution in a bent flexible photonic chip simulated using FEM: when the multilayer is subject to concave bending, FEM results clearly show that the strain distribution is not monotonic across the stack thickness. Both compressive and tensile strains are present in the PI and SU-8 layers, which is contradictory to Eq. S2 where only one neutral axis exists in the structure.

© 2014 Macmillan Publishers Limited. All rights reserved.

DOI: 10.1038/NPHOTON.2014.138

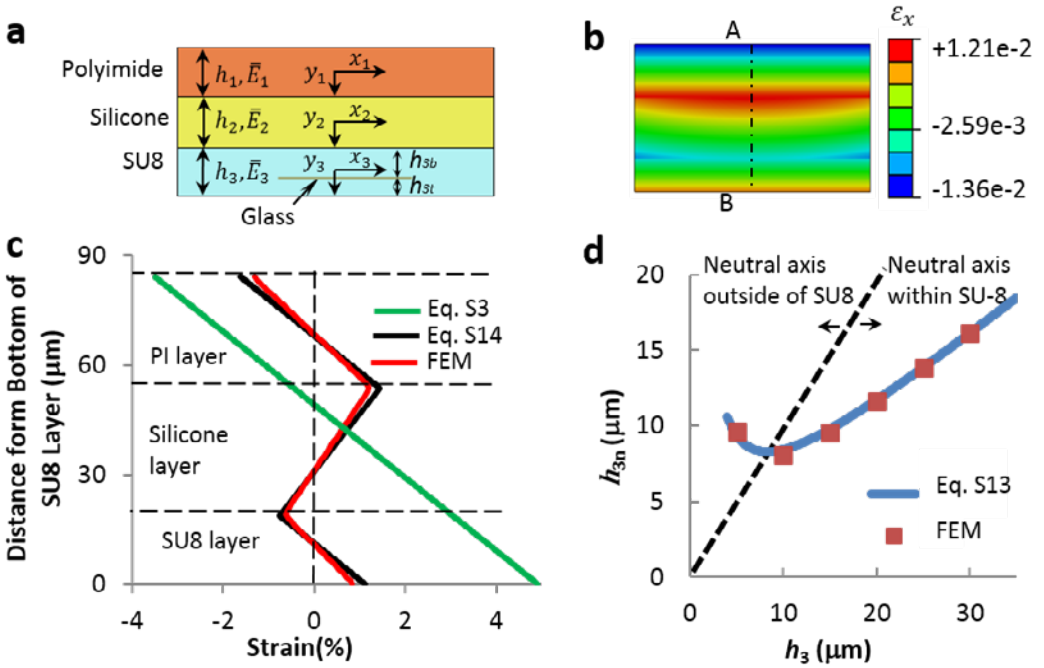

Figure S6 | Multi-neutral-axis theory. **a**, Cross-sectional schematic of the flexible photonic chip, with a PI-silicone-SU8 three-layer structure (not drawn to scale), thickness and plane strain Young's modulus are as labelled, and the local coordinate originates from the median plane of each layer. **b**, Contour plot of bending strain distribution obtained from FEM when the structure in Fig. S6a is bent. **c**, Through-stack strain distribution in the flexible chip with an SU-8 layer thickness of 18.9 μm when bent to a radius of 1 mm: the green line represents results calculated using the conventional theory (Eq. S3), the black curve is derived using our multiple neutral-axes theory (Eq. S14), and the red curve are FEM simulations. **d**, the position of SU-8 neutral axis from SU-8 surface as a function of SU-8 thickness. The blue curve comes from Eq. S13 and the solid markers are FEM results. Dash line denotes the boundary of SU-8. When the h_3 is smaller than the critical value of 8.28 μm, the neutral axis will shift outside SU-8 to the left hand side of the dash line and hence is not accessible to the device.

To accurately predict the strain distribution in each layer, we assume that the cross-sectional planes in PI and those in SU-8 remain planar during bending. Therefore, linear relation between strain and curvature (Eq. S3) is still valid.

The coordinate system we adopt is depicted in Fig. S6a, with notations given in Table S4.

© 2014 Macmillan Publishers Limited. All rights reserved.

Table S4 | Notations used in the mechanical modelling

Layer	Young's Modulus	Thickness	Strain distribution	Distance from neutral axis to median plane	Distance from neutral axis to bending centre
PI	$\bar{E}_1$	h_1	$\epsilon_1(y_1)$	d_1	ρ_1
silicone	$\bar{E}_2$	h_2	$\epsilon_2(y_2)$	--	--
SU-8	$\bar{E}_3$	h_3	$\epsilon_3(y_3)$	d_3	ρ_3

Our goal is to find an analytical solution for d_3 so that we know where to place the photonic devices for minimum strain.

Using the local coordinate systems, strain in PI can be written as:

$$\epsilon_1(y_1) = \frac{y_1 - d_1}{\rho_1} \left(-\frac{h_1}{2} < y_1 < \frac{h_1}{2}\right) \tag{S4}$$

Strain in the SU-8 layer is

$$\epsilon_3(y_3) = \frac{y_3 - d_3}{\rho_3} \left(-\frac{h_3}{2} < y_3 < \frac{h_3}{2}\right) \tag{S5}$$

We suppose that strain in silicone layer is a linear function of y_2 as inspired by our FEM results:

$$\epsilon_2(y_2) = ay_2 + b \left(-\frac{h_2}{2} < y_2 < \frac{h_2}{2}\right) \tag{S6}$$

where a and b are coefficients to be determined by continuity conditions at PI/silicone and silicone/SU-8 interfaces.

Continuity at layer interfaces imposes:

$$\begin{cases} \epsilon_2\left(-\frac{h_2}{2}\right) = \epsilon_1\left(\frac{h_1}{2}\right) \\ \epsilon_2\left(\frac{h_2}{2}\right) = \epsilon_3\left(-\frac{h_3}{2}\right) \end{cases} \tag{S7}$$

Force equilibrium in *x* direction imposes:

$$\bar{E}_1 \int_{-\frac{h_1}{2}}^{\frac{h_1}{2}} \frac{y_1 - d_1}{\rho_1} dy + \bar{E}_3 \int_{-\frac{h_3}{2}}^{\frac{h_3}{2}} \frac{y_3 - d_3}{\rho_3} dy_3 + \bar{E}_2 \int_{-\frac{h_2}{2}}^{\frac{h_2}{2}} (ay_2 + b) dy_2 = 0 \tag{S8},$$

Combing Eqs. S7 and S8 yields a relation between d_1 and d_3:

$$2\left(\frac{\bar{E}_1 h_1 d_1}{\rho_1} + \frac{\bar{E}_3 h_3 d_3}{\rho_3}\right) = \bar{E}_2 h_2 \left(\frac{\frac{h_1}{2} - d_1}{\rho_1} - \frac{\frac{h_3}{2} + d_3}{\rho_3}\right) \tag{S9}$$

which satisfies the following two extreme cases: (i) When E_2=0, i.e. there is no material layer between PI and SU-8, both d_1 and d_3 should go to zero. (ii) When $\bar{E}_1 = \bar{E}_2 = \bar{E}_3$, i.e. the composite beam decays to a beam of uniform material, there should be only one neutral axis, i.e. $d_1 = \frac{h_2 + h_3}{2}$ and $d_3 = -\frac{h_1 + h_2}{2}$.

Assuming PI and SU-8 have the same original length and the same bending angle, the

© 2014 Macmillan Publishers Limited. All rights reserved.

DOI: 10.1038/NPHOTON.2014.138

bending radius from each layer's neutral axis to its bending centre should also be the same, which means

$$\rho_1 = \rho_3 \tag{S10}$$

Substituting Eq. S10 into Eq. S9 yields:

$$2(\bar{E}_1 h_1 d_1 + \bar{E}_3 h_3 d_3) = \bar{E}_2 h_2 \left((\frac{h_1}{2} - d_1) - (\frac{h_3}{2} + d_3) \right) \tag{S11}$$

As shown in Table S4, $\bar{E}_2 \ll \bar{E}_1$ and $\bar{E}_2 \ll \bar{E}_3$, which implies that the right hand side of Eq. S11 is much smaller than the left hand side and can be approximated as zero, hence

$$d_3 = -d_1 \frac{\bar{E}_1 h_1}{\bar{E}_3 h_3} \tag{S12}$$

For a constant PI thickness, our FEM results have validated a hypothesis that due to the soft silicone interlayer, the thickness of SU-8 has little effect on the position of the neutral axis of PI layer as long as SU-8 is thinner or of comparable thickness to the PI. We may then take d_1 as a constant and by fitting the FEM results, we obtain $d_1 = 0.836$ μm.

The distance from SU-8 surface to SU-8 neutral axis h_{3n} is thus given by:

$$h_{3\mathrm{n}} = \frac{h_3}{2} + d_1 \frac{\bar{E}_1 h_1}{\bar{E}_3 h_3} \tag{S13}$$

where d_1 = 0.836 μm is the distance from the PI neutral axis to the PI median plane, which is found to be a constant when silicone thickness is fixed. In a single free-standing SU-8 layer, $h_{3\mathrm{n}} = h_3/2$. When SU-8 is bonded to PI via silicone adhesive, the effect of PI is captured by the second term in Eq. S13: the thicker the PI layer (i.e. the larger h_1), the further away the neutral axis of SU-8 from its median plane.

Once the neutral axes are determined, strain distribution across the stack thickness is given by

$$\varepsilon = \begin{cases} \frac{y_1 - d_1}{\rho} & \left(-\frac{h_1}{2} \le y_1 < \frac{h_1}{2} \right) \\ \frac{(\frac{h_2}{2} - y_1)(\frac{h_1}{2} - d_1) - (\frac{h_2}{2} + y_1)(\frac{h_3}{2} + d_3)}{\rho h_2} & \left(-\frac{h_2}{2} \le y_2 < \frac{h_2}{2} \right) \\ \frac{y_3 - d_3}{\rho} & \left(-\frac{h_3}{2} \le y_3 \le \frac{h_3}{2} \right) \end{cases} \tag{S14}$$

where ρ represents the average radius of the multilayer. Results from the conventional bending theory (Eq. S3), FEM, and our new multi-neutral-axis model (Eq. S14) are compared in Fig. S6c. Conventional bending theory predicts monotonic linear strain distribution whereas both FEM and Eq. S14 capture non-monotonic strain distribution in the multilayer stack. Linear strain

© 2014 Macmillan Publishers Limited. All rights reserved.

distribution in each layer obtained from FEM further corroborates our basic assumptions. The locations of zero strain plane for different SU-8 thicknesses calculated using Eq. S13 are plotted in Fig. S6d. The dashed curve in Fig. S6d represents the equation $h_{3n} = h_3$. When h_3 < 8.28 μm, the neutral axis will locate outside the SU-8 layer and hence no longer accessible for device placement.

© 2014 Macmillan Publishers Limited. All rights reserved.

DOI: 10.1038/NPHOTON.2014.138

VI. *In*-situ strain-optical coupling characterization method

Fig. S7a schematically illustrates the flexible chip testing setup. To facilitate optical coupling into the single-mode waveguides, the 0.8 μm wide bus waveguides are tapered to a width of 2 μm near their end facets. The fibre-to-waveguide coupling loss is not optimized in this work and is estimated to be approximately 4 dB per facet. Fig. S7b shows a far-field image of quasi-TE guided mode output from a single-mode $Ge_{23}Sb_7S_{70}$ glass waveguide on a plastic substrate and Fig. S7c shows a photo of a flexible chip under bending test. The chip was glued onto the linear motion sample stages using double-sided sticky tapes. Bending radius of the flexible chip was measured from the image using an imaging processing software (Image J).

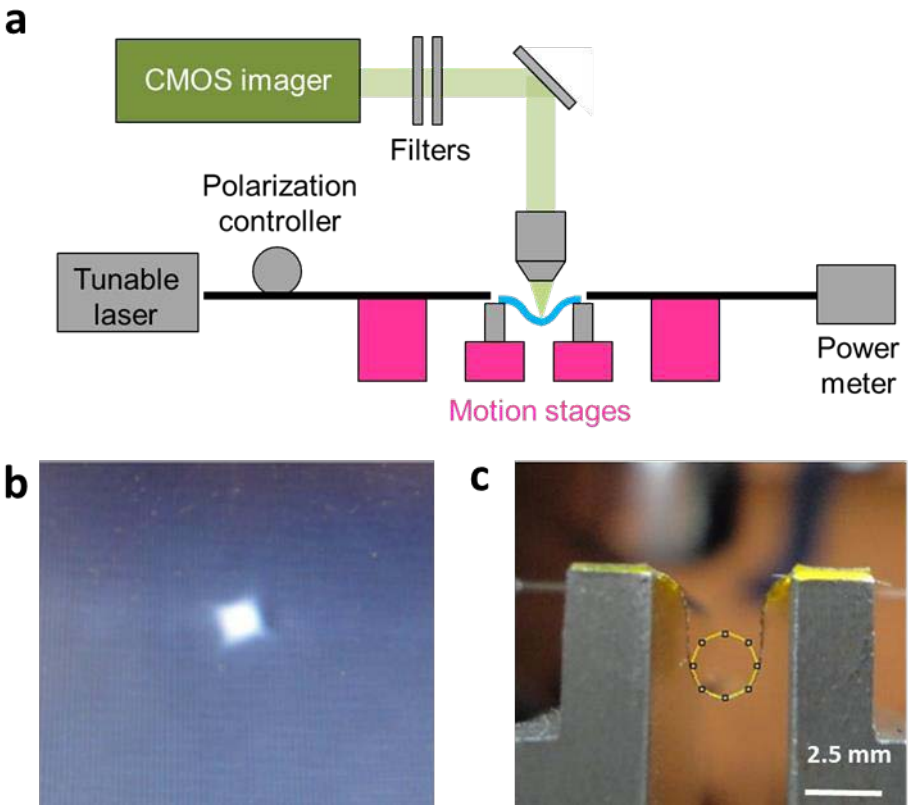

Figure S7 | a, Schematic diagram of the testing setup. **b**, Far-field image of TE guided mode output from a single-mode flexible $Ge_{23}Sb_7S_{70}$ glass waveguide. **c**, Photo of a flexible waveguide chip under bending test: an imaging processing software was used to extract the bending radius of the chip from the image.

© 2014 Macmillan Publishers Limited. All rights reserved.

VII. Strain-optical coupling theory

This Part of Supplementary Material aims to derive Eq. 1, which governs the strain-optical coupling properties in flexible photonic resonant cavity devices.

The resonant condition of a resonant cavity device can be generally given by:

$$N\lambda = n_{eff}L \tag{S15}$$

when strain introduces a perturbation to the resonant wavelength λ, we have:

$$N(\lambda + d\lambda) = n_{eff}L + d\left(n_{eff}L\right) = n_{eff}L + Ldn_{eff} + n_{eff}dL \tag{S16}$$

The effective index change dn_{eff} originates from two mechanisms: the strain-optical material response, as well as the cross-sectional geometry change of the resonator due to strain:

$$dn_{eff} = \sum_i \Gamma_i \left(\frac{dn}{d\varepsilon}\right)_i d\varepsilon + \frac{dn_{eff}}{d\varepsilon}d\varepsilon + \frac{dn_{eff}}{d\lambda}d\lambda \tag{S17}$$

Here the first term corresponds to the material contribution, and the second term only takes into account the geometric change. The coefficient $dn_{eff}/d\varepsilon$ can be calculated once the local strain at the resonator is known using the perturbation theory involving shifting material boundaries[12]. The third term results from effective index dispersion in the resonator: as the resonant wavelength shifts, the corresponding effective index also changes. Combining the two equations leads to Eq. 1. Note that the group index in Eq. 1 is defined as:

$$dn_{eff} = n_{eff} - d\lambda\frac{dn_{eff}}{d\lambda} \tag{S18}$$

© 2014 Macmillan Publishers Limited. All rights reserved.

DOI: 10.1038/NPHOTON.2014.138

VIII. Optimized 3-D photonic device design parameters

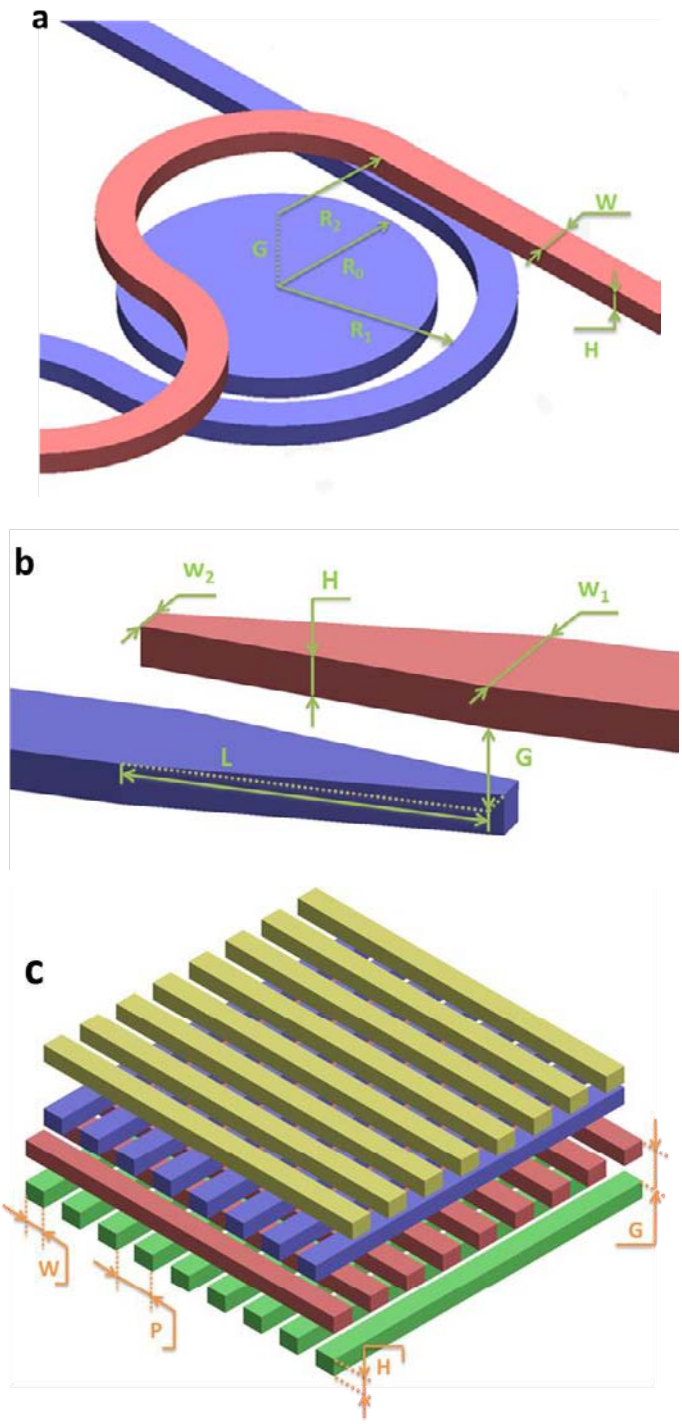

Figure S8 | Schematic structures of 3-D photonic devices. a, a two-layer vertically coupled resonator. **b**, An interlayer waveguide couplers. **c**, A woodpile photonic crystal. The key geometric parameters are labelled in the figures.

© 2014 Macmillan Publishers Limited. All rights reserved.

Table S5 | Optimized 3-D photonic device geometric parameters.

Fig. S8a	W	H	R_0	R_1	R_2	G
(μm)	0.8	0.4	30	30.8	29.4	0.9
Fig. S8b	W_1	W_2	L	H	G	
(μm)	0.9	0.6	40	0.4	0.55	
Fig. S8c	W	P	H	G		
(μm)	1.5	3	0.36	0.8		

A set of 3-D photonic devices with varied design parameters were fabricated and tested. Table S5 summarizes the experimentally determined geometric parameter combinations that yield the optimized performance presented in this study.

© 2014 Macmillan Publishers Limited. All rights reserved.

DOI: 10.1038/NPHOTON.2014.138

IX. Scattering matrix formalism for calculating the transfer function of vertically coupled add-drop filters

The vertically coupled add-drop filter can be treated using a circuit model[13] shown in Fig. S9. The power coupling coefficients between the resonator and the add and drop port waveguides are given by K_1 and K_2, respectively. Power loss due to coupling is neglected in the calculation. L is the resonator circumference and α is the optical loss in the micro-disk resonator. Using the scattering matrix method, loaded quality factor Q_{load}, maximum power at the drop port and minimum power at the through port at resonance can be obtained by the equations:

$$Q_{load} = \frac{2\pi n_g L}{\lambda_r (K_1 + K_2 + (1-\sigma^2))} \tag{S19}$$

$$I_{drop-max} = I_{in} \frac{K_1 K_2 \sigma^2}{(1-\sigma\sqrt{1-K_1}\sqrt{1-K_2})^2} \tag{S20}$$

$$I_{through-min} = I_{in} \frac{(\sqrt{1-K_1}-\sigma\sqrt{1-K_2})^2}{(1-\sigma\sqrt{1-K_1}\sqrt{1-K_2})^2} \tag{S21}$$

where λ is the resonant wavelength, I_{in} is the input power, σ is the intrinsic amplitude loss in one round trip and is expressed as

$$\sigma = \exp(-1/2\ \alpha L) \tag{S22}$$

n_g is the group index of the resonator and can be defined as follows:

$$n_g = c_0/(FSR \cdot L) \tag{S23}$$

Here, c_0 is the light speed in vacuum, and FSR is the free spectral range (FSR) of the resonator in the frequency domain. Based on the measured transmission spectrum (Fig. 4b) and the equations above, the coupling coefficients can be fitted, which in turn allows the prediction of the resonator transmission spectrum. The parameters used in the calculation are listed in Table S6.

The intrinsic quality factor (Q_{in}) of the micro-disk resonator is 1.9×10^5 calculated using[14]

$$Q_{in} = \frac{2\pi n_g}{\alpha\lambda} \tag{S24}$$

which is consistent with that of all-pass resonators we fabricated using the same method.

© 2014 Macmillan Publishers Limited. All rights reserved.

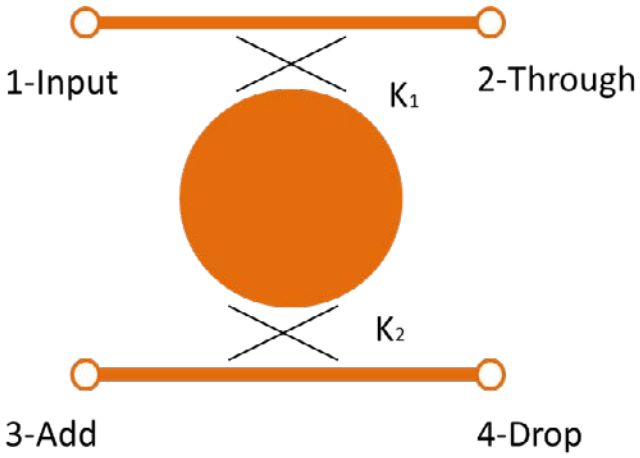

Figure S9 | Schematic illustration of a circuit model of the vertically coupled add/drop filter.

Table S6 | Parameters used to calculate the transmission spectrum of the vertically coupled add/drop resonator filter shown in Fig. 4c.

L(um)	λ_r(nm)	I_{in} (nW)	I_0 (nW)	I_{thmin} (nW)	I_{drmax} (nW)	Q_{load}
188.5	1566.228	87.7	3.2	4.4	67.3	2.2×10^4
FSR(GHZ)	n_g	K_1	K_2	σ	α(dB/cm)	Q_{in}
757	2.10	0.041	0.024	0.996	2.0	1.9×10^5

© 2014 Macmillan Publishers Limited. All rights reserved.

DOI: 10.1038/NPHOTON.2014.138

X. Woodpile photonic crystal diffraction experiment configurations

Fig. S10 illustrates the diffraction experiment setup. Monochromatic green light from a collimated 532 nm diode-pumped solid state green laser was incident at an angle θ = 45 degrees upon the surface of the PhC sample, and the diffraction patterns were projected onto a white board perpendicular to the (0 0) specular order reflection. To calculate the projected positions of different diffraction orders, the wave vector can be decomposed in the coordinate system shown in Fig. S10, where the x and z axes are in-plane with the woodpile PhC structure while the y axis is perpendicular to the PhC sample surface. For the (0 0) specular order, the wave vector is:

$$\vec{k}_{(0\,0)} = \left(k_{x0}, k_{y0}, 0\right) = (k_0 cos\theta, k_0 sin\theta, 0) \tag{S25}$$

where k_0 is the wave vector in vacuum. For a diffraction spot of the (n m) order, its wave vector is:

$$\vec{k}_{(n\,m)} = \left(k_x, k_y, k_z\right) = (k_{x0} + \mathrm{n}\, G_x, \sqrt{k_0^2 - k_x^2 - k_z^2}, \mathrm{m}\, G_z\,) \tag{S26}$$

according to the Bragg diffraction equation, where G_x, G_z are the PhC in-plane reciprocal lattice vectors. Thus the diffraction angle of the (n m) order light with respect to the (0 0) order can be calculated using:

$$\alpha = \arctan\left(\frac{k_x}{k_y}\right) - \theta \tag{S27}$$

$$\beta = \arctan\left(\frac{k_z}{\sqrt{k_x^2 + k_y^2}}\right) \tag{S28}$$

and the position of the (n m) order pattern in the x'-y' plane (on the white board) is written as:

$$(\mathrm{D}\tan\alpha\ , \mathrm{D}\ \tan\beta\ /\cos\alpha)$$

Diffraction patterns predicted using the approach agree well with the experimental results, as shown in Fig. 5b.

© 2014 Macmillan Publishers Limited. All rights reserved.

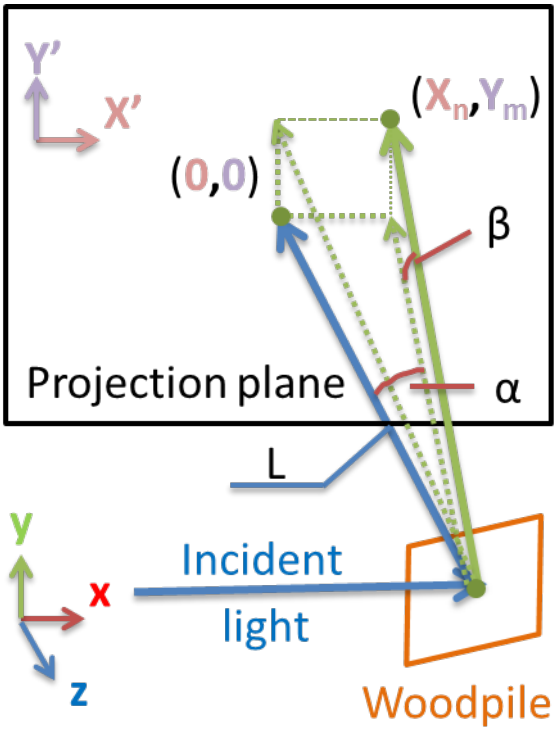

Figure S10 | Schematic diagram illustrating the experimental setup used to map the diffracting patterns from the woodpile photonic crystal structure.

© 2014 Macmillan Publishers Limited. All rights reserved.

DOI: 10.1038/NPHOTON.2014.138

References:

1. Zhang, Y., Lin, C.T. & Yang, S. Fabrication of Hierarchical Pillar Arrays from Thermoplastic and Photosensitive SU-8. *small* **6**, 768-775 (2010).
2. Roelkens, G. *et al*. Adhesive bonding of InP/InGaAsP dies to processed silicon-on-insulator wafers using DVS-bis-benzocyclobutene. *Journal of the Electrochemical Society* **153**, G1015-G1019 (2006).
3. Schiltz, A. AN EMPIRICAL-MODEL FOR PLANARIZATION WITH POLYMER-SOLUTIONS. *Japanese Journal of Applied Physics Part 1-Regular Papers Short Notes & Review Papers* **34**, 4185-4194 (1995).
4. Xiao, S., Khan, M.H., Shen, H. & Qi, M. Modeling and measurement of losses in silicon-on-insulator resonators and bends. *Optics Express* **15**, 10553-10561 (2007).
5. Hu, J. *et al*. Si-CMOS-compatible lift-off fabrication of low-loss planar chalcogenide waveguides. *Optics Express* **15**, 11798-11807 (2007).
6. Kwak, K., Cho, K. & Kim, S. Stable Bending Performance of Flexible Organic Light-Emitting Diodes Using IZO Anodes. *Scientific Reports* **3**, 2787 (2013).
7. Chou, C.H., Chuang, J.K. & Chen, F.C. High-Performance Flexible Waveguiding Photovoltaics. *Scientific Reports* **3**, 2244 (2013).
8. Park, S. *et al*. Flexible molecular-scale electronic devices. *Nature Nanotechnology* **7**, 438-442 (2012).
9. Munzenrieder, N. *et al*. Flexible a-IGZO TFT amplifier fabricated on a free standing polyimide foil operating at 1.2 MHz while bent to a radius of 5 mm. in *Electron Devices Meeting (IEDM), 2012 IEEE International* 5.2.1-5.2.4 (2012).
10. El-Kady, M.F., Strong, V., Dubin, S. & Kaner, R.B. Laser Scribing of High-Performance and Flexible Graphene-Based Electrochemical Capacitors. *Science* **335**, 1326-1330 (2012).
11. Jong-Hyun, A. *et al*. High-speed mechanically flexible single-crystal silicon thin-film transistors on plastic substrates. *Electron Device Letters, IEEE* **27**, 460-462 (2006).
12. Johnson, S.G. *et al*. Perturbation theory for Maxwell's equations with shifting material boundaries. *Physical Review E* **65** (2002).
13. Schwelb, O. Transmission, group delay, and dispersion in single-ring optical resonators and add/drop filters - A tutorial overview. *Journal of Lightwave Technology* **22**, 1380-1394 (2004).
14. Hu, J. Planar halcogenide glass materials and devices. *Ph.D. thesis* (2009).

© 2014 Macmillan Publishers Limited. All rights reserved.